nature materials

Article

https://doi.org/10.1038/s41563-024-01952-7

Quadrupling the depairing current density in the iron-based superconductor $SmFeAsO_{1-x}H_x$

Received: 28 August 2023

Accepted: 20 June 2024

Published online: 18 July 2024

Check for updates

Masashi Miura [1,2,3] ✉, Serena Eley [4,5], Kazumasa Iida [6], Kota Hanzawa[7], Jumpei Matsumoto[7], Hidenori Hiramatsu[7,8], Yuki Ogimoto [1], Takumi Suzuki [1], Tomoki Kobayashi [9], Toshinori Ozaki[10], Hodaka Kurokawa[11], Naoto Sekiya[12], Ryuji Yoshida [13], Takeharu Kato[13], Tatsunori Okada [14], Hiroyuki Okazaki[15], Tetsuya Yamaki[15], Jens Hänisch [16], Satoshi Awaji[14], Atsutaka Maeda[9], Boris Maiorov [2] & Hideo Hosono [8,17]

Iron-based 1111-type superconductors display high critical temperatures and relatively high critical current densities J_c. The typical approach to increasing J_c is to introduce defects to control dissipative vortex motion. However, when optimized, this approach is theoretically predicted to be limited to achieving a maximum J_c of only ~30% of the depairing current density J_d, which depends on the coherence length and the penetration depth. Here we dramatically boost J_c in $SmFeAsO_{1-x}H_x$ films using a thermodynamic approach aimed at increasing J_d and incorporating vortex pinning centres. Specifically, we reduce the penetration depth, coherence length and critical field anisotropy by increasing the carrier density through high electron doping using H substitution. Remarkably, the quadrupled J_d reaches 415 MA cm^{-2}, a value comparable to cuprates. Finally, by introducing defects using proton irradiation, we obtain high J_c values in fields up to 25 T. We apply this method to other iron-based superconductors and achieve a similar enhancement of current densities.

Superconductors have attracted technological interest partially due to their extremely high dissipation-free current densities J_c. In these materials, the superconducting current is carried by electron pairs that can be broken apart if the current surpasses the depairing current density J_d, which sets the ultimate limit on the achievable J_c. A considerable challenge at the convergence between fundamental and applied superconductivity research is determining what structural and chemical properties are required to reach this maximum and how J_c depends on parent or competing phases in the magnetic phase diagram. The critical current can be severely restricted by dissipation triggered by the motion of vortices, magnetic flux lines that penetrate type-II superconductors. Accordingly, most research efforts to increase J_c have focused on adding material defects, creating spatial inhomogeneities in the free energy and therefore preferential positions for vortices to localize (pin) to reduce their core energies[1–3]. Consequently, the defect landscape defines a vortex pinning potential $U_{act}(J, H, T)$ that depends on the current density J, magnetic field $\mu_0 H$ where μ_0 is the permeability in vacuum and H is the magnetic field strength, temperature T and disorder.

When optimized, this approach of core pinning alone may achieve a maximum J_c of only ~30% of J_d. The argument for this specific limit first considers how, to immobilize vortices, the effective pinning force imparted by the collective action of defects must balance out the force induced by the current. It then finds that the maximum pinning force f_p^{core} imposed by pinning vortex cores (reducing the vortex energy by the condensation energy) is only ~30% that of the driving

A full list of affiliations appears at the end of the paper. ✉e-mail: masashi-m@st.seikei.ac.jp

https://doi.org/10.1038/s41563-024-01952-7

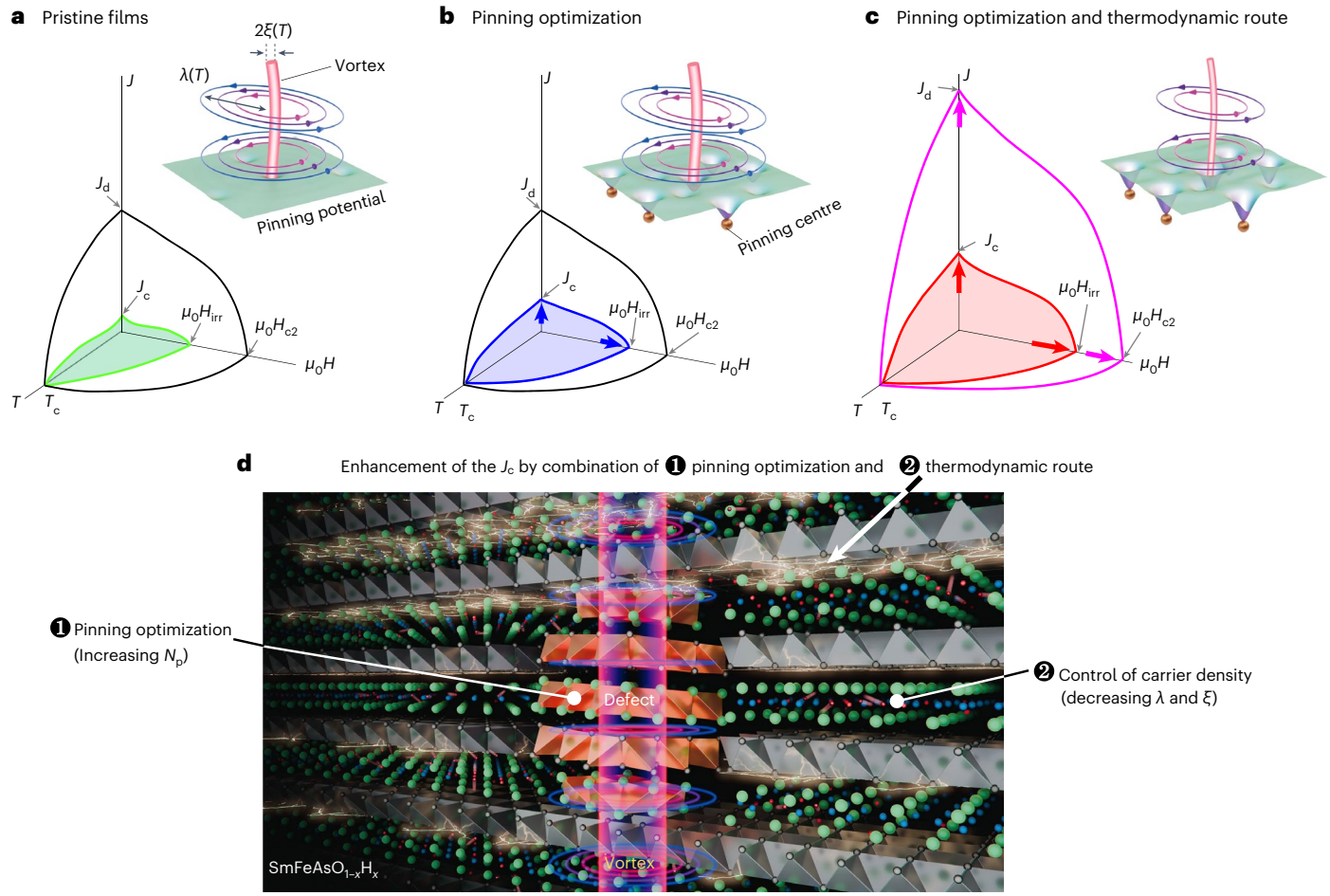

Fig. 1 | Evolution of the phase diagram of superconductors after pinning optimization and tuning the carrier density. The J–H–T phase diagrams for superconductors. **a**, As-grown films. **b**, Films after incorporating defects to pin vortices (pinning optimization). **c**, Films after a combined method of tuning the carrier density (thermodynamic route) and pinning optimization. Note that vortex pinning also occurs in the as-grown film, based on the intrinsic defect landscape. The insets depict a vortex navigating a pinning landscape in each scenario. **d**, A schematic of the microstructure resulting from the combined approach. N_p, density of pinning centres.

force f_d induced from a current equivalent to J_d, such that $f_p^{core}/f_d \approx 30\%$ (refs. 4–6). (As such, a J_c near J_d has been achieved only in a nanomesh system precluding vortex formation, but this architecture is not scalable for large-scale applications[7].) Most materials achieve critical currents far below this ceiling given the challenges associated with optimizing this pinning potential—notably, incorporating defects without straining the interlaying superconducting matrix and inadvertently suppressing J_c or the critical temperature T_c.

Here we present a somewhat new paradigm for boosting J_c. We propose targeting increasing J_d to raise the ceiling—denoted the thermodynamic approach—while concurrently engineering the defect landscape to approach this higher upper limit—collectively referred to herein as the combined approach. The comparative J–H–T phase diagrams are shown in Fig. 1. From Fig. 1a, we see that pristine films typically have small spatial variations in the potential energy landscape, leading to easy vortex motion and therefore a low J_c/J_d ratio. Figure 1b captures how incorporating defects deepens the wells (U_{act}) that vortices must overcome to move. Here, U_{act} depends on the type of pinning, for example, strong pinning, in which a large defect can independently impart sufficient force on a vortex to immobilize it, or weak collective pinning, in which atomic-scale defects act collectively to immobilize segments of a vortex[8,9]. Accordingly, the J_c/J_d ratio increases, reaching a maximum at ~30%—a value achieved in few studies—balanced with the challenge of avoiding degradation in T_c. Lastly, our combined approach is illustrated in Fig. 1c,d. The energy wells deepen not only from defects, but also from fundamentally changing the vortex structure, affecting the condensation energy. By increasing J_d, higher J_c values are achieved, even if the J_c/J_d ratio is maintained compared to values from defect engineering alone.

Regarding how to tune J_d, we turn to Ginzburg–Landau theory[10], which derives the temperature dependence of the depairing current density as

$$J_d(T) = \Phi_0 / \left[3\sqrt{3}\pi\mu_0 \xi(T)(\lambda(T))^2\right] \propto n_s(T), \quad (1)$$

where Φ_0 is the flux quantum, μ_0 is the permeability in vacuum, ξ is the coherence length, λ is the penetration depth and n_s is the superfluid density. The vortex structure depends on two parameters: the vortex core diameter is ~$2\xi(T)$ and it is surrounded by supercurrents of radius up to $\lambda(T)$. From equation (1), we see that a dramatic reduction in the penetration depth would induce a concomitantly substantial increase in J_d. The penetration depth depends inversely on the superfluid density n_s as $\lambda \propto \sqrt{m^*/n_s}$, where m^* is the effective mass. Hence, we can tune λ by controlling the carrier density through doping—the thermodynamic route.

To identify appropriate candidates to implement this route for optimizing J_c, we consider the T_c–doping phase diagrams, which can host a variety of phases outside of the superconducting phase.

https://doi.org/10.1038/s41563-024-01952-7

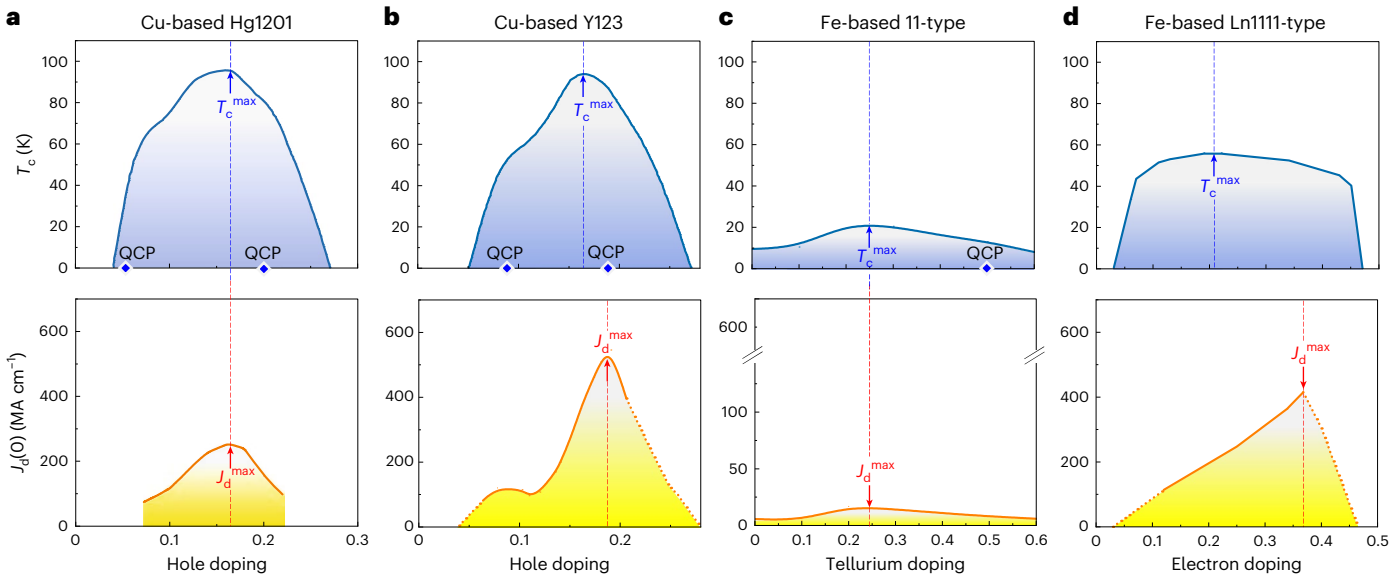

Fig. 2 | Carrier density dependence of T_c and J_d. a–d, Dependence of T_c (top panel) and J_d (bottom panel) for Cu-based Hg1201 (**a**; refs. 12,13), Cu-based Y123 (**b**; refs. 3,16,17), Fe-based 11-type (**c**; refs. 14,15) and Fe-based *Ln*1111-type (**d**; refs. 18,19) superconductors. The solid curves represent measurements from the citations, whereas the dashed segments in **a**, **b** and **d** (bottom panel) are from our unpublished data. Note that J_d in **d** is calculated based on λ and ξ, which are experimentally obtained in this work (Fig. 3). Notice that, for the *Ln*1111-type Fe-based material, though the peaks in J_d (J_d^{max}) and T_c (T_c^{max}) do not occur at the same doping level, the broad T_c–doping dome enables sufficiently high doping to reach the J_d peak with a minimal decrease in T_c from its maximum. The QCP in the 11-type superconductor has been observed only in a bulk sample[14].

From the T_c–doping phase diagrams, illustrated in Fig. 2, we must identify materials in which the predicted increase in J_d (Supplementary Table 1) is not accompanied by a rapid decrease in T_c. For materials that follow the Uemura plot[11] (that is, $T_c \propto 1/\lambda^2$), T_c and J_d should apex at the same carrier density because both parameters are proportional to $1/\lambda^2$. We show examples of this in Fig. 2a,c for the moderately anisotropic Cu-based $HgBa_2CuO_{4+\delta}$ (Hg1201) superconductor[12,13] and nearly isotropic Fe-based $FeSe_{1-x}Te_x$ (11-type) superconductor[14,15], respectively. On the other hand, Fig. 2b,d shows example results from a Cu-based $YBa_2Cu_3O_y$ (Y123) sample[3,16,17] and an Fe-based $SmFeAsO_{1-x}H_x$ (a *Ln*1111-type) sample (*Ln* is a lanthanoid element)[18,19] in which J_d and T_c do not peak at the same doping level, but rather J_d peaks in the highly doped region because of a non-concurrent dip in λ and peak in T_c with carrier density.

From Fig. 2b,d, we identify Y123 and *Ln*1111-type iron-based superconductors as ideal candidates for our combined approach because T_c remains nearly maximal when J_d peaks in the high doping regime. Based on this, we have previously demonstrated extremely high J_c values in $(Y_{0.77}Gd_{0.23})Ba_2Cu_3O_y$ films using our proposed approach, by precisely tuning J_d through controlling the carrier concentration and then incorporating nanoparticles[3] to pin vortices. We achieved a critical current density reaching ~32.4% of J_d at 4.2 K. From Fig. 2b, we now observe that the peak in J_d coincides with a quantum critical point (QCP)—a sudden change in the n_s and effective mass m^*. This is quite interesting; the presence of QCPs should have a dramatic impact on J_d and J_c, providing partial motivation for studying the doping dependence of J_c in multiple categories of superconductors.

In this study we test our combined approach in iron-based superconductors, with a focus on a *Ln*1111-type material. We successfully achieve very high self-field J_c ($J_c^{s.f.}$) and in-field J_c values as well as pinning force densities F_p for $SmFeAsO_{1-x}H_x$ films—among the highest reported for iron-based superconductors. Specifically, at 4.2 K, the samples demonstrate a $J_c^{s.f.} \approx 16.11$ MA cm^{-2} and in-field J_c(25 T) = 3.01 MA cm^{-2}, corresponding to F_p(25 T) ≈ 750 GN m^{-3}, with the latter two measured in an out-of-plane field (**H** ∥ *c*) of 25 T. Additionally, we apply a new method of increasing the carrier concentration well into the highly doped regime by doping with hydrogen[20], beyond what is achievable using the traditional method of doping with fluorine. This enables tuning into a regime in which we calculate a maximum in $J_d(T = 0)$ of 415 MA cm^{-2} (Fig. 2d), surpassed only by overdoped Y123 (refs. 3,21). We further successfully apply this approach to other iron-based superconductors. In $FeSe_{1-x}Te_x$ films, we find that J_c at 4.2 K increases from 0.29 to 1.43 MA cm^{-2} due to the increase in $J_d(0)$ by a factor of 3.0. Moreover, for $BaFe_2(As_{1-x}P_x)_2$ films, J_c at 4.2 K increases from 0.45 to 3.55 MA cm^{-2} due to the increase in $J_d(0)$ by a factor of 5.0.

H doping and proton irradiation of SmFeAsO films

For this study we first grew 50-nm-thick films of the parent compound SmFeAsO by pulsed laser deposition on MgO substrates and then doped them with hydrogen. To substitute H^- for a fraction of the O^{2-} sites, we performed a topotactic chemical reaction using CaH_2 powder. This enabled us to increase the carrier density into the highly doped regime—with a high H concentration reaching ~35% of O sites, higher than that achieved with F doping (<20%). Film preparation process details have been published elsewhere[20,22]. Next we analysed the depth dependence of the H concentrations (*x* in Supplementary Fig. 1). Lastly we irradiated some samples to induce artificial nano-defects (Methods for details).

Figure 3 compares the microstructure of pristine and irradiated $SmAsFeO_{0.632}H_{0.368}$ films, displaying scanning transmission electron microscope (STEM) images and elemental maps (through energy dispersive spectroscopy, EDS) in Fig. 3a,c and Fig. 3b,d, respectively. The STEM image shows that the pristine $SmAsFeO_{0.632}H_{0.368}$ film is epitaxial, without discernible defects. In Fig. 3b, the EDS maps of Sm, Fe and As indicate that the film is homogeneous. Figure 3c reveals several nano-sized defects aligned with the *c* axis and *ab* plane, defects that were induced by the proton irradiation process. In Fig. 3d, from the EDS maps we observe some small compositional variations mostly aligned along the *c* axis that appear rich in Fe and poor in Sm and As.

Figure 4a presents the phase diagram for pristine and irradiated films. For reference, the data from $SmFeAsO_{1-x}H_x$ bulk samples are

https://doi.org/10.1038/s41563-024-01952-7

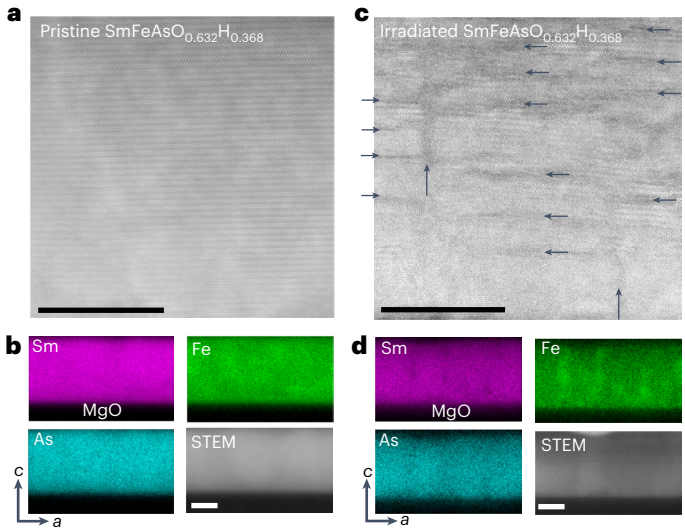

Fig. 3 | Microstructure of a $SmFeAsO_{1-x}H_x$ thin film (x = 0.368) grown epitaxially on MgO. a, Cross-sectional STEM image of the pristine film. **b**, Elemental maps of the pristine film and low-magnification STEM image. Sm, Fe and As were homogeneously distributed in the matrix; maps collected using EDS. **c**, STEM image of the film after proton irradiation, revealing that irradiation introduced defects oriented along both the *c* axis and *ab* plane. **d**, Elemental maps and low-magnification STEM image of the irradiated film. All scale bars, 20 nm. The vertical and horizontal arrows indicate the nano-sized defects.

also plotted[19]. The T_c and J_c values were measured using a four-probe method; data are shown in Supplementary Fig. 2a,b, respectively. The films also demonstrate little sensitivity of T_c to electron concentration (x in Fig. 4; e, electron in this figure), and irradiation reduces T_c by only 0.4 K for both $SmAsFeO_{0.661}H_{0.339}$ and $SmAsFeO_{0.632}H_{0.368}$ films. Figure 4b shows the carrier density (n) at 50 K as a function of x for the pristine and irradiated films obtained from Hall measurements (Supplementary Fig. 3). For a comparison, n values for other *Ln*1111-type bulk samples are plotted[23]. The n in the $SmFeAsO_{1-x}H_x$ films increases with increasing x. The $J_c^{s.f.}$ at 4.2 K increases with carrier doping beyond that achieved by F doping, as shown in Fig. 4c. Even though the pristine and irradiated films have almost the same dependence of T_c and carrier density n on carrier doping x, the $J_c^{s.f.}$ of the irradiated $SmFeAsO_{1-x}H_x$ films is 1.75 times higher than that in the pristine film. This is because n, T_c and ξ of the interlaying superconducting matrix, between defect clusters, are unaltered by irradiation. The J_c values in the irradiated $SmAsFeO_{0.632}H_{0.368}$ films ($J_c^{s.f.}$(4.2 K) = 16.11 MA cm^{-2}) are the same order of magnitude as those of $NdFeAsO_{1-x}H_x$ films[24] and an irradiated $SmFeAsO_{1-x}F_x$ single crystal[25]. Supplementary Table 2 compares T_c, n and $J_c^{s.f.}$ values for the pristine versus irradiated films.

Tuning the depairing current density

In Fig. 4d,e, we show how the in-plane coherence length, ξ_{ab} and in-plane penetration depth, λ_{ab} vary with carrier doping. Figure 4d displays $\xi_{ab}(T=0)$ as a function of x for our films. The coherence length ξ_{ab} is typically calculated from measurements of the temperature-dependent upper critical field, H_{c2}, that is, $\mu_0 H_{c2}(T) = \phi_0/2\pi(\xi_{ab}(T))^2$, in which $H_{c2}(0)$ and therefore $\xi_{ab}(0)$ are extracted from an extrapolation of a fit to an appropriate model, given the inability to access fields up to $H_{c2}(0)$. The Werthamer–Helfand–Hohenberg formula[26] is most commonly applied, though in its original form it strictly models the case of single-band superconductors. Here we apply the Gurevich two-band model in the clean limit[27] to fit the experimental $H_{c2}(T)$ data. We find that most of our $H_{c2}(T)$ data fit well to this model, and that the $SmAsFeO_{0.632}H_{0.368}$ film exhibits a downward curvature in $H_{c2}(T)$ over a very narrow range of temperatures (within 2% of T_c) that notably deviates from the fit. An in-depth discussion of the fits, speculation on the cause of the downturn in one sample, temperature-dependent resistivity data from which H_{c2} is extracted (Supplementary Fig. 4) and the fits (Supplementary Figs. 5 and 6 and Supplementary Table 3) are included in the Supplementary Information. For reference, $\xi_{ab}(0)$ values from the literature for other doped *Ln*1111-type materials are included[24,28,29]. The calculated $\xi_{ab}(0)$ of the $SmAsFeO_{0.632}H_{0.368}$ films decreases with increasing x, with the pristine and irradiated $SmAsFeO_{0.632}H_{0.368}$ achieving the lowest $\xi_{ab}(0)$ value, which is close to the doping level of a possible QCP in $NdFeAsO_{1-x}H_x$ (ref. 30). Interestingly, local minima of $\xi_{ab}(0)$ at the two QCPs have been reported for Y123 (ref. 17). Next, to determine the penetration depth $\lambda_{ab}(T=0)$, we use the temperature dependence of the resonant frequency of the coplanar waveguide resonators (detailed in Supplementary Fig. 7). As shown in Fig. 4e, we see that $\lambda_{ab}(0)$ of $NdFeAsO_{1-x}H_x$ films decreases with increasing x, which is a similar trend to that of other doped *Ln*1111-type materials[31–33], indicating there are thermodynamic changes occurring with H doping.

Figure 4f displays the calculated $J_d(0)$ within Ginzburg–Landau theory[10] for other doped *Ln*1111-type materials. The zero-temperature depairing current density $J_d(0)$ for the $SmFeAsO_{1-x}H_x$ films increases with n, reaching a maximum at a large value of 415 MA cm^{-2}. This is among the highest J_d for any superconductor, surpassed by overdoped Y123 ($J_d(0) \approx 500$ MA cm^{-2}) and higher than that of Hg1201 ($J_d(0) = 280$ MA cm^{-2}). Supplementary Table 1 shows a comparison of J_d in multiple superconductors. Because T_c typically correlates with J_d, it is also remarkable that a material with half the T_c of Y123 and Hg1201 produces a similar J_d. For our film with maximum doping, the J_d enhancement is one of the main reasons for the higher J_c, as shown in Fig. 4c.

High in-field critical current density

The field dependence of J_c at 4.2 K for **H** ∥ *c* for pristine and irradiated $SmAsFeO_{0.632}H_{0.368}$ films is summarized in Fig. 5a, with data for other superconductors included. First, the irradiated $SmAsFeO_{0.632}H_{0.368}$ film, irradiated $SmFeAsO_{1-x}F_x$ (ref. 25) and $Ba_{1-x}K_xFe_2As_2$ (ref. 34) all have similar $J_c^{s.f.}$ values. However, J_c for the latter two samples degrades rapidly with increasing field, such that both the pristine and irradiated $SmAsFeO_{0.632}H_{0.368}$ films demonstrate the highest J_c for fields above ~3.5 T. Second, proton-irradiated $SmAsFeO_{0.632}H_{0.368}$ improves the in-field J_c, reaching a high J_c value for iron-based superconductors[24,25,28,34]. In fact, the in-field J_c in this film surpasses that of optimally doped Y123 (ref. 35), although it remains lower than the current record value, which was achieved in an overdoped Y123 film containing nanoparticles[3].

The remarkable in-field performance achieved by H doping and subsequently irradiating the $SmAsFeO_{0.632}H_{0.368}$ film is highlighted in the pinning force density (F_p) plot in Fig. 5b. For **H** ∥ *c*, F_p for the pristine $SmAsFeO_{0.632}H_{0.368}$ film reaches a maximum at 20 T and then decreases for higher fields. Consistent with the increase in J_c, F_p for the irradiated $SmAsFeO_{0.632}H_{0.368}$ film increased for all applied fields and orientations measured; F_p at 25 T increased by a factor of 1.7 upon irradiation. The F_p for the irradiated $SmAsFeO_{0.632}H_{0.368}$ film does not saturate up to 25 T, as a result of the improved $J_c(H)$ due to enhanced vortex pinning by proton irradiation. Moreover, for both **H** ∥ *c* and **H** ∥ *ab*, the irradiated $SmAsFeO_{0.632}H_{0.368}$ film has a roughly 1.5 times higher J_c compared to that in pristine film at all fields up to 25 T, as seen in the Fig. 5b inset.

Reduced upper critical field anisotropy

For many materials, F_p peaks and then dramatically decreases with increasing magnetic field. However, our irradiated $SmAsFeO_{0.632}H_{0.368}$ film maintains a relatively high F_p up to high magnetic fields, which is promising for high-field applications. Moreover, our samples have two additional desirable characteristics for applications: relatively low upper critical field anisotropy and consequently a J_c that is insensitive to field orientation. Specifically, in Fig. 5c, we show the H_{c2} anisotropy $\gamma_H = H_{c2}(||ab)/H_{c2}(||c)$, which was determined from the in-field resistivity

https://doi.org/10.1038/s41563-024-01952-7

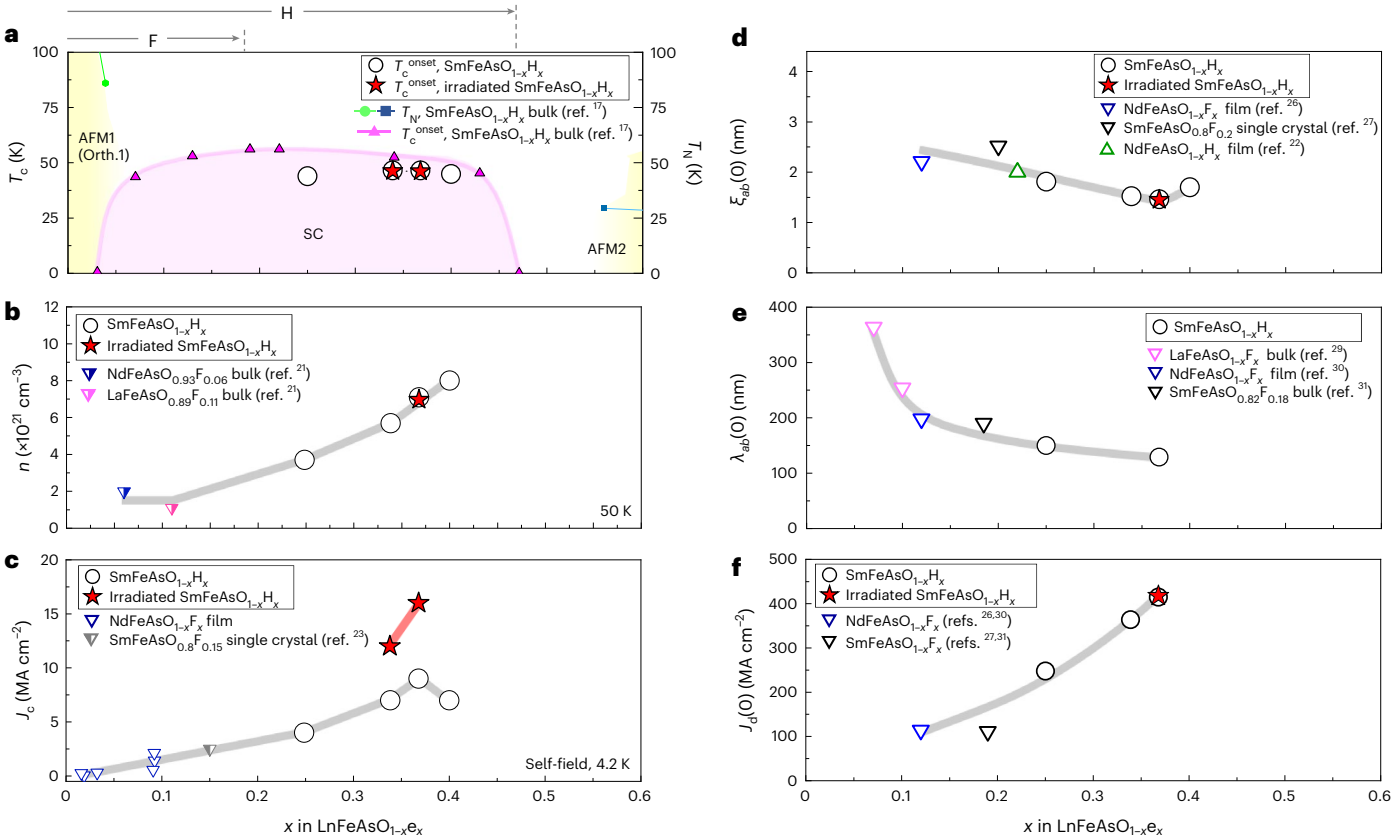

Fig. 4 | Physical quantities as a function of electron doping (per Fe). a, Phase diagram of SmFeAsO. There is a single T_c dome and two antiferromagnetic phases (AFM1 and AFM2) near $x < 0.05$ and $x > 0.55$ (ref. 19). At the top of panel **a**, the arrow labeled F indicates the range of electron doping accessible by doping with fluorine, whereas the arrow labeled H indicates the range accessible by doping with hydrogen. Here, SC refers to the superconducting phase, Orth.1 refers to the structural transition from the tetragonal to the orthorhombic phase, T_N is the Néel temperature and T_c^{onset} is the onset of the critical temperature. **b**, Carrier density n at 50 K for $SmFeAsO_{1-x}H_x$ films and $LnFeAsO_{1-x}F_x$ (ref. 23). **c**, Self-field J_c at 4.2 K. For a comparison, the data for $NdFeAsO_{1-x}F_x$ and $SmFeAsO_{1-x}F_x$ (ref. 25) are superimposed. **d**, Zero-temperature in-plane coherence length $\xi_{ab}(0)$ evaluated from the slope of the upper critical field for $SmFeAsO_{1-x}H_x$ films and $LnFeAsO_{1-x}e_x$ (refs. 24,28,29). **e**, Zero-temperature in-plane penetration depth $\lambda_{ab}(0)$ measured by the superconducting resonator method. For a comparison, the data for $LnFeAsO_{1-x}F_x$ (refs. 31–33) are plotted. **f**, Zero-temperature depairing current density $J_d(0)$ calculated by equation (1); $\xi_{ab}(0)$ and $\lambda_{ab}(0)$ were taken from **d** and **e**. For the irradiated films, $\lambda_{ab}(0)$ for the pristine film was used to calculate J_d. In **b**–**d**, the grey lines are guides to the eye highlighting the trends in each parameter with changes in doping, and the red line highlights the trend for the irradiated sample.

measurements. Compared with the $LnFeAsO_{1-x}F_x$ sample, the γ_H values of our $SmFeAsO_{1-x}H_x$ films are substantially smaller, a fact that originates from the increased dimensionality of the Fermi surface[36]. Specifically, F-doped *Ln*1111-type materials have two-dimensional Fermi surfaces containing hole and electron pockets, whereas H doping induces a three-dimensional hole pocket[36]. In fact, the resulting difference in anisotropy is rather remarkable at $T/T_c \approx 0.8$, where F doping results in an anisotropy of ~4–5 (refs. 28,37), which is halved in the highly doped regime by H doping. Such a reduction in anisotropy by doping has not been achieved in Y123, which has anisotropies of 5.5, 5.1 and 4.3 for underdoping[3], optimal doping[38] and overdoping[3], respectively. Additionally, the H_{c2} anisotropy depends on temperature, which is not observed in Y123 data but has been seen in other iron-based superconductors[28,37,39–41] (Fig. 5c).

We can also see the consequences of both reduced anisotropy and irradiation in our angle (θ)-dependent critical current density measurements, shown in Fig. 5d. Comparing the two pristine $SmAsFeO_{0.751}H_{0.249}$ and $SmAsFeO_{0.632}H_{0.368}$ films, the $SmAsFeO_{0.632}H_{0.368}$ film has a higher $J_c(\theta)$ and a smaller anisotropy of J_c ($\gamma_{J_c} = J_c^{ab}/J_c^{c}$). This is due to the high $J_c^{s.f.}$ and small anisotropy of both H_{c2} (Supplementary Fig. 9a,b) and the irreversibility field (H_{irr}; Supplementary Fig. 9c,d), a result of high hydrogen doping. Moreover, for the irradiated H-doped $SmAsFeO_{0.632}H_{0.368}$ film, an increase in J_c at all applied magnetic field orientations and an enhancement of H_{irr} are achieved (Supplementary Fig. 9c), which is a combined effect of high H doping, as well as defects aligned with the *c* axis and *ab* plane, introduced by proton irradiation. This is favourable over defects of a singular orientation, such as *c*-axis-aligned defects[1,42], which produce a large peak at **H** ∥ *c*.

Slowing vortex creep by reducing the Ginzburg parameter

While the maximum achievable J_c increases by increasing J_d, our technique also reduces the vortex creep rates (S) in hole-doped Y123, 11-type, P-doped 122-type and electron-doped *Ln*1111-type films. For the *Ln*1111-type system, we specifically demonstrated this in Nd1111 samples of different doping levels as well as in a highly doped Sm1111 film. This is important because fast creep can decrease J_c and induced persistent currents. Our method not only increases J_c, but also targets decreasing the Ginzburg number $\mathrm{Gi} \propto T_c^2\gamma_H^2\lambda_{ab}^4/\xi_{ab}^2$, which parameterizes the impact of thermal fluctuations and positively correlates with creep rates[43].

Figure 6a shows S versus $1/\mathrm{Gi}^{1/2}$ at $T = T_c/4$ and 1 T for various superconductors. First, reducing Gi in each material system reduces S. For example, the $SmAsFeO_{0.632}H_{0.368}$ film shows smaller S compared to that in the $NdFeAsO_{1-x}e_x$ films, which is due to the reduction of Gi, notably by reducing $\lambda_{ab}(0)$ and γ_H. Second, adding defects also slows creep.

https://doi.org/10.1038/s41563-024-01952-7

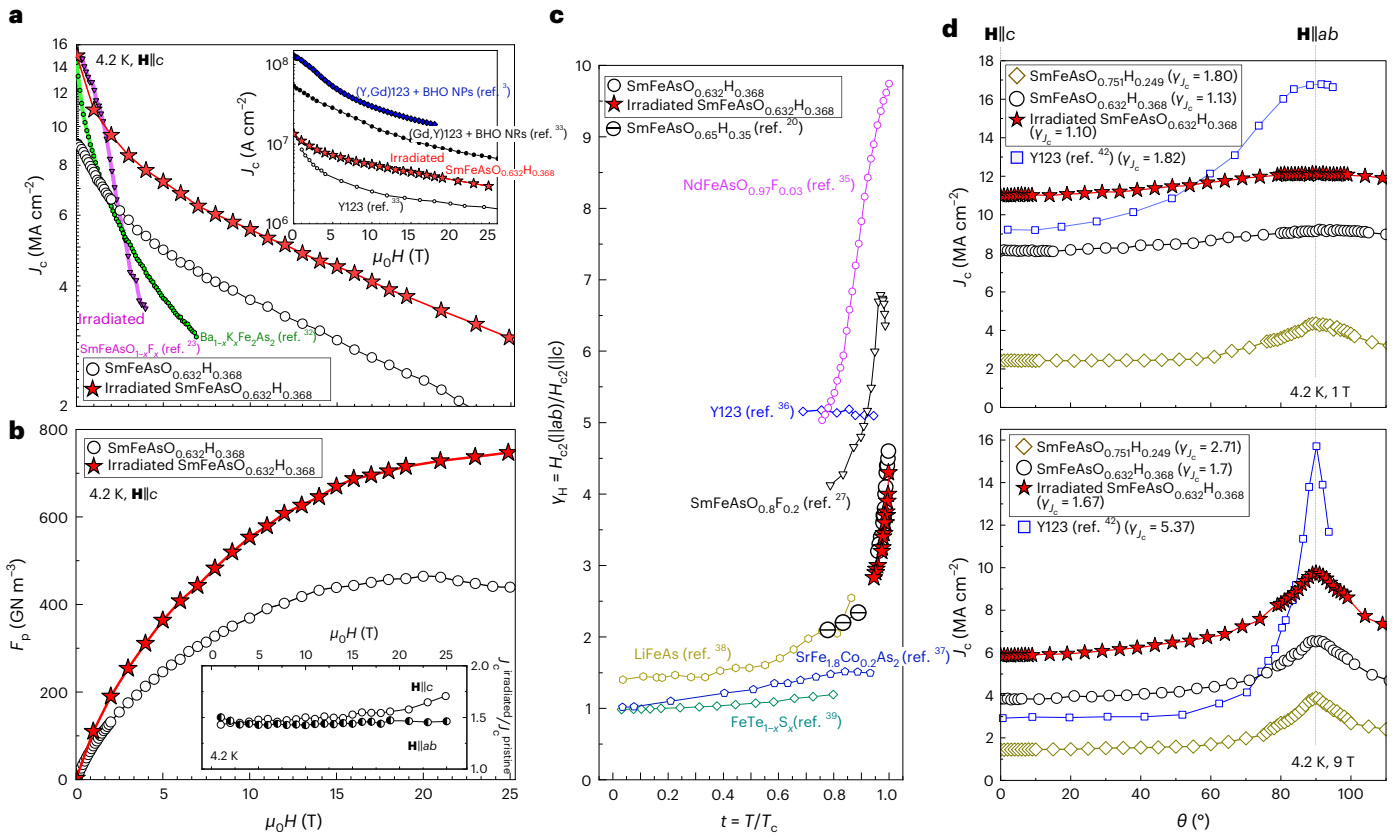

Fig. 5 | In-field superconducting properties of the pristine and irradiated SmFeAsO$_{0.632}$H$_{0.368}$ samples. a, A comparison of the field dependent J_c for pristine and irradiated SmFeAsO$_{1-x}$H$_x$ films, an irradiated SmFeAsO$_{1-x}$F$_x$ crystal[25] and a Ba$_{1-x}$K$_x$Fe$_2$As$_2$ film[34]. The inset in **a** compares results for the irradiated H-doped Sm1111 film to data for an overdoped (Y,Gd)123 conductor containing BaHfO$_3$ nanoparticles (BHO NPs)[3], a Y123 conductor[35] and (Gd,Y)123 with BaHfO$_3$ nanorods (NRs)[35], showing that J_c in the SmFeAsO$_{1-x}$H$_x$ is higher than in the Y123 conductor. **b**, F_p for the pristine SmFeAsO$_{0.632}$H$_{0.368}$ showed a peak of ~420 GN m^{-3} at around 20 T. After irradiation, the maximum F_p was 740 GN m^{-3} at around 25 T. The enhancement in J_c after irradiation as a function of the applied field is shown in the inset in **b**. The ratio of J_c after irradiation ($J_c^{irradiated}$) to J_c before ($J_c^{pristine}$) was calculated using the data shown in Supplementary Fig. 8. Notice that the enhancement is maintained up to the highest applied magnetic field for both field orientations. **c**, Anisotropy of H_{c2} for the SmFeAsO$_{0.632}$H$_{0.368}$ films as a function of reduced temperature (t). Here, $H_{c2}(||ab)$ and $H_{c2}(||c)$ are the upper critical field values when the field is applied parallel to the ab-plane and c-axis, respectively. The γ_H was slightly reduced by the proton irradiation. For a comparison, the data for NdFeAsO$_{0.97}$F$_{0.03}$ (ref. 37), Y123 (ref. 38), SrFe$_{1.8}$Co$_{0.2}$As$_2$ (ref. 39), LiFeAs (ref. 40), FeTe$_{1-x}$S$_x$ (ref. 41), SmFeAsO$_{0.65}$H$_{0.35}$ (ref. 22) and SmFeAsO$_{0.8}$F$_{0.2}$ (ref. 29) are included. Compared to NdFeAsO$_{0.97}$F$_{0.03}$ (ref. 37) and SmFeAsO$_{0.8}$F$_{0.2}$ (ref. 29), SmFeAsO$_{0.632}$H$_{0.368}$ shows lower γ_H. **d**, Angular dependence of J_c at 4.2 K and 1 T (top) as well as 9 T (bottom) for various SmFeAsO$_{1-x}$H$_x$ films. The anisotropy of J_c is calculated as $\gamma_{J_c} = J_c^{ab}/J_c^{c}$ for each sample, which is indicated in the legend. Compared to Y123 (ref. 44), the γ_{J_c} of SmFeAsO$_{0.632}$H$_{0.368}$ is very small, especially at 9 T. After irradiation, J_c increased in SmFeAsO$_{0.632}$H$_{0.368}$ for all field orientations.

For technical reasons, we were unable to measure S for the irradiated SmAsFeO$_{0.632}$H$_{0.368}$ films, owing to a small sample volume; nevertheless, we expect reduced S as achieved in the other materials.

Discussion

The standard method of increasing J_c—focusing exclusively on introducing either weak collective pinning centres or strong pinning centres—typically has little effect on the penetration depth. A major advantage of our thermodynamic approach is that our ability to reduce the penetration depth λ has a dramatic effect on both Gi and J_d because $Gi^{1/2} \approx \lambda^2$ and $J_d \approx 1/\lambda^2$. Consequently, the advantages associated with reduced λ in SmFeAsO$_{1-x}$H$_x$ are further enhanced by the high calculated values for J_d, achieved using this method, and we demonstrate substantial increases in J_d in many materials. Figure 6b therefore summarizes the main achievements of this work, displaying our measurements of the in-field J_c ($H = 1$ T, and $\mathbf{H} \parallel c$) as a function of J_d at 4.2 K for Y123 and three classes of iron-based superconductors with varied pinning landscapes. Details of the calculation parameters for J_d and experimentally obtained J_c are shown in Supplementary Table 4. First, we see that J_c tends to positively correlate with J_d. Note that SmFeAsO$_{1-x}$H$_x$ also reduced the creep rate (compared to the NdFeAsO$_{1-x}$e$_x$ films), which may have contributed to the increased J_c in this material. Second, we see that for the pristine SmFeAsO$_{1-x}$H$_x$ films, J_c(4.2 K) at 1 T and $\mathbf{H} \parallel c$ increases from 3.1 to 7.0 MA cm^{-2}, correlated with an increase in J_d tuned by the electron concentration. Third, at 4.2 K and 1 T for $\mathbf{H} \parallel c$, the combination of tuning J_d and adding a high density of nano-defects produces an in-field J_c of 11 MA cm^{-2} and a corresponding J_c/J_d of 3.1% (where J_d(4.2 K) = 360 MA cm^{-2}) that is comparable to the pristine Y123 conductor[44].

In the introduction, we discussed the coincidence between the peak in J_d and a QCP in Y123. Such correspondence is unsurprising. Because $J_d(T) \approx 1/\lambda^2 \propto n_s/m^*$ and if the n_s diverges around the QCP, there may be a precipitous dip in the doping-dependent λ, engendering an apex in J_d, therefore enabling an unprecedentedly high J_c. However, the behaviour of λ at the QCP, or more generally with doping, depends on the relative rate of change of the effective mass versus n_s, and this behaviour does not appear to be universal. Consistent with our study, a dip in λ was captured in a hole-doped cuprate (related to pseudo-gap formation)[45]. On the other hand, in BaFe$_2$(As$_{1-x}$P$_x$)$_2$ (ref. 46) and Ba(Fe$_{1-x}$Co$_x$)$_2$As$_2$ (ref. 47), a sharp peak in λ appears at the QCP. Regarding Ln1111-type superconductors, although a QCP has been

https://doi.org/10.1038/s41563-024-01952-7

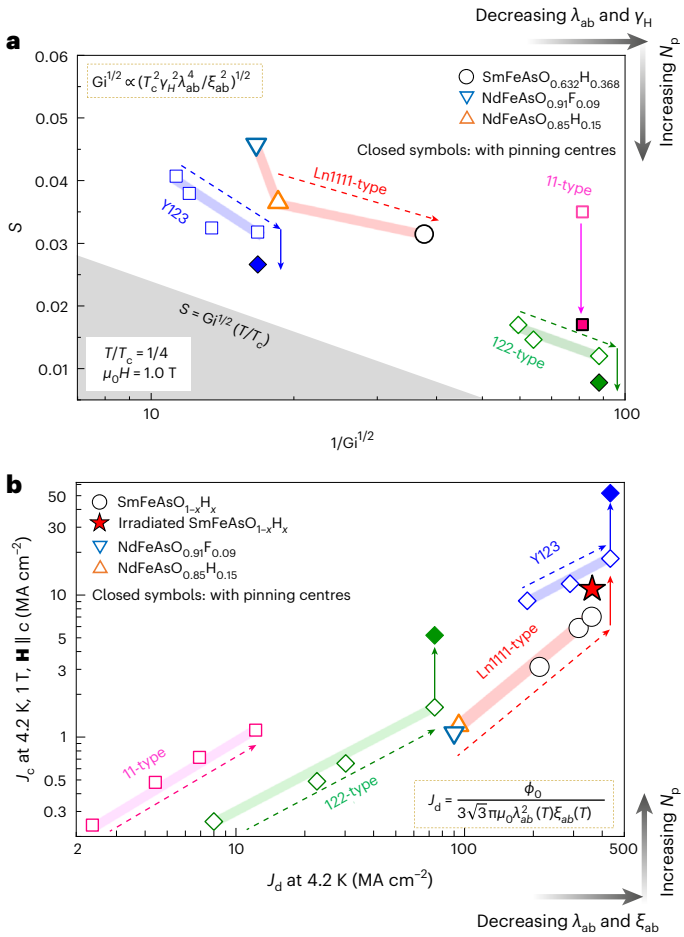

Fig. 6 | Dependence of S and J_c versus J_d after tuning various superconducting parameters. a, Flux creep rate S as a function of $Gi^{-1/2}$ at $t = T/T_c = 0.25$ and 1 T for Y123 and three classes of iron-based superconductors. Data for the 11-type material (FeSe) is from the literature[50]. Increasing electron concentration decreases S for $SmFeAsO_{0.632}H_{0.368}$. This tendency was also observed for $YBa_2Cu_3O_y$ with increased hole concentration[3] and $BaFe_2(As_{1-x}P_x)_2$ with increased chemical pressure. The grey region indicates ranges of S below the predicted lower limit[43], indicated by the equation $S = Gi^{1/2}(T/T_c)$. **b**, In-field J_c as a function of the depairing current density J_d at 4.2 K and 1 T. Increasing carrier concentration by increasing electron and hole doping as well as chemical pressure enhances J_d in all displayed classes of superconductors. Additional enhancement can be achieved by the introduction of pinning centres. Closed symbols show data for samples containing vortex pinning centres (nanoparticle inclusions or irradiation-induced defects). Each coloured wide line connects the data within each class of material and the dashed arrows show how S (**a**) is decreased and J_c (**b**) is increased as our tuning parameter (doping or chemical pressure) increases. The coloured solid arrows show the changes in S (**a**) and J_c (**b**) upon adding vortex pinning centers (open symbols are data for pristine sample whereas solid symbols are for sample containing pinning centers).

found in $LaFeAsO_{1-x}H_x$ (ref. 48) and evidence of a possible QCP in $NdFeAsO_{1-x}H_x$ has been discussed[30], no QCP has yet been found in other *Ln*1111-type materials. Given the potential for extremely high J_c values at QCPs, further studies of the relationship between QCPs and J_d are warranted.

In summary, using a combined approach of tuning J_d by controlling λ and ξ through the tuning of the carrier density and enhancing flux pinning by irradiation, we substantially boost J_c in $SmFeAsO_{1-x}H_x$ films. Our films showed very high in-field J_c values in iron-based superconductors. This increase should by no means be the maximum achievable J_c in $SmFeAsO_{1-x}H_x$; for Y123, ~15% of J_d has been reported in a field of 3 T, and 32.4% of J_d has been reported at self-field[3], near the predicted maximum that is achievable with core pinning[4–6,49]. Consequently, the remarkably high J_d of 415 MA cm^{-2} that we achieved sets a new ceiling for J_c in $SmFeAsO_{1-x}H_x$ films. Further studies are warranted to fully optimize pinning in this material. Our methods also reduce the effective mass anisotropy γ and Gi, resulting in slower vortex creep. We have therefore demonstrated that this combined approach is effective in improving the performance of superconductors of different families: hole-doped cuprates (Y123)[3] and iron-based superconductors (electron-doped *Ln*1111-type, Te-doped 11-type and chemically pressured P-doped 122-type[3]).

Online content

Any methods, additional references, Nature Portfolio reporting summaries, source data, extended data, supplementary information, acknowledgements, peer review information; details of author contributions and competing interests; and statements of data and code availability are available at https://doi.org/10.1038/s41563-024-01952-7.

References

1. MacManus-Driscoll, J. L. et al. Strongly enhanced current densities in superconducting coated conductors of $YBa_2Cu_3O_{7-x}$ + $BaZrO_3$. *Nat. Mater.* **3**, 439–443 (2004).
2. Gutiérrez, J. et al. Strong isotropic flux pinning in $YBa_2Cu_3O_{7-x}$ + $BaZrO_3$ films derived from chemical solutions. *Nat. Mater.* **6**, 367–373 (2007).
3. Miura, M. et al. Thermodynamic approach for enhancing superconducting critical current performance. *npg Asia Mater.* **14**, 85 (2022).
4. Matsushita, T. *Flux Pinning in Superconductors* (Springer-Verlag, 2007).
5. Gurevich, A. Pinning size effects in critical currents of superconducting films. *Supercond. Sci. Technol.* **20**, S128–S135 (2007).
6. Wimbush, S. C. *Applied Superconductivity* Ch. 1, 1–104 (John Wiley & Sons, 2015).
7. Xu, K., Cao, P. & Heath, J. R. Achieving the theoretical depairing current limit in superconducting nanomesh films. *Nano Lett.* **10**, 4206–4210 (2010).
8. Larkin, A. I. & Ovchinnikov, Y. N. Pinning in type II superconductors. *J. Low Temp. Phys.* **34**, 409–428 (1979).
9. Blatter, G., Geshkenbein, V. B. & Koopmann, J. A. G. Weak to strong pinning crossover. *Phys. Rev. Lett.* **92**, 067009 (2004).
10. Tinkham, M. *Introduction to Superconductivity* 2nd edn (McGraw-Hill, 1996).
11. Uemura, Y. J. et al. Universal correlations between T_c and n_s/m^* (carrier density over effective mass) in high-T_c cuprate superconductors. *Phys. Rev. Lett.* **62**, 2317–2320 (1989).
12. Hofer, J. et al. Doping dependence of superconducting parameters in $HgBa_2CuO_{4+\delta}$ single crystals. *Phys. C Supercond.* **297**, 103–110 (1998).
13. Chan, M. K. et al. Extent of Fermi-surface reconstruction in the high-temperature superconductor $HgBa_2CuO_{4+\delta}$. *Proc. Natl Acad. Sci. USA* **117**, 9782–9786 (2020).
14. Ishida, K. et al. Pure nematic quantum critical point accompanied by a superconducting dome. *Proc. Natl Acad. Sci. USA* **119**, e2110501119 (2022).
15. Kurokawa, H. et al. Relationship between superconductivity and nematicity in $FeSe_{1-x}Te_x$ (x = 0 – 0.5) films studied by complex conductivity measurements. *Phys. Rev. B* **104**, 014505 (2021).
16. Ramshaw, B. J. et al. Quasiparticle mass enhancement approaching optimal doping in a high-T_c superconductor. *Science* **348**, 317–320 (2015).
17. Grissonnanche, G. et al. Direct measurement of the upper critical field in cuprate superconductors. *Nat. Commun.* **5**, 3280 (2014).

18. Iimura, S. et al. Large-moment antiferromagnetic order in overdoped high-T_c superconductor $^{154}SmFeAsO_{1-x}D_x$. *Proc. Natl Acad. Sci. USA* **11**, E4354–E4359 (2017).
19. Hosono, H., Yamamoto, A., Hiramatsu, H. & Ma, Y. Recent advances in iron-based superconductors toward applications. *Mater. Today* **21**, 278–302 (2018).
20. Matsumoto, J. et al. Superconductivity at 48 K of heavily hydrogen-doped SmFeAsO epitaxial films grown by topotactic chemical reaction using CaH_2. *Phys. Rev. Mater.* **3**, 103401 (2019).
21. Stangl, A., Palau, A., Deutscher, G., Obradors, X. & Puig, T. Ultra-high critical current densities of superconducting $YBa_2Cu_3O_{7-\delta}$ thin films in the overdoped state. *Sci. Rep.* **11**, 8176 (2021).
22. Hanzawa, K. et al. High upper critical field (120 T) with small anisotropy of highly hydrogen-substituted SmFeAsO epitaxial film. *Phys. Rev. Mater.* **6**, L111801 (2022).
23. Jaroszynski, J. et al. Comparative high-field magnetotransport of the oxypnictide superconductors $RFeAsO_{1-x}F_x$ (R = La, Nd) and $SmFeAsO_{1-\delta}$. *Phys. Rev. B* **78**, 064511 (2008).
24. Kondo, K. et al. NdFeAs(O,H) epitaxial thin films with high critical current density. *Supercond. Sci. Technol.* **33**, 09LT01 (2020).
25. Fang, L. et al. Huge critical current density and tailored superconducting anisotropy in $SmFeAsO_{0.8}F_{0.15}$ by low-density columnar-defect incorporation. *Nat. Commun.* **4**, 2655 (2013).
26. Werthamer, N. R., Helfand, E. & Hohenberg, P. C. Temperature and purity dependence of the superconducting critical field, H_{c2}. III. Electron spin and spin-orbit effects. *Phys. Rev.* **147**, 295–302 (1966).
27. Gurevich, A. Iron-based superconductors at high magnetic fields. *Rep. Prog. Phys.* **74**, 124501 (2011).
28. Kauffmann-Weiss, S. et al. Microscopic origin of highly enhanced current carrying capabilities of thin NdFeAs(O,F) films. *Nanoscale Adv.* **1**, 3036–3048 (2019).
29. Lee, H. S. et al. Effects of two gaps and paramagnetic pair breaking on the upper critical field of $SmFeAsO_{0.85}$ and $SmFeAsO_{0.8}F_{0.2}$ single crystals. *Phys. Rev. B* **80**, 144512 (2009).
30. Chen, M. Y. et al. Inter- to intra-layer resistivity anisotropy of NdFeAs(O,H) with various hydrogen concentrations. *Phys. Rev. Mater.* **6**, 054802 (2022).
31. Luetkens, H. et al. Field and temperature dependence of the superfluid density in $LaFeAsO_{1-x}F_x$ superconductors: a muon spin relaxation study. *Phys. Rev. Lett.* **101**, 097009 (2008).
32. Talantsev, E. F. et al. *p*-wave superconductivity in iron-based superconductors. *Sci. Rep.* **9**, 14245 (2019).
33. Drew, A. J. et al. Coexistence of magnetic fluctuations and superconductivity in the pnictide high temperature superconductor $SmFeAsO_{1-x}F_x$ measured by muon spin rotation. *Phys. Rev. Lett.* **101**, 097010 (2008).
34. Iida, K. et al. Approaching the ultimate superconducting properties of $(Ba,K)Fe_2As_2$ by naturally formed low-angle grain boundary networks. *npg Asia Mater.* **13**, 68 (2021).
35. Xu, A. et al. Strongly enhanced vortex pinning from 4 to 77 K in magnetic fields up to 31 T in 15 mol.% Zr-added (Gd, Y)-Ba-Cu-O superconducting tapes. *APL Mater.* **2**, 046111 (2014).
36. Muraba, Y., Matsuishi, S. & Hosono, H. Enhancing the three-dimensional electronic structure in 1111-type iron arsenide superconductors by H substitution. *Phys. Rev. B* **89**, 094501 (2014).
37. Jaroszynski, J. et al. Upper critical fields and thermally-activated transport of $NdFeAsO_{0.7}F_{0.3}$ single crystal. *Phys. Rev. B* **78**, 174523 (2008).
38. Miura, M. et al. Upward shift of the vortex solid phase in high-temperature superconducting wires through high density nanoparticle addition. *Sci. Rep.* **6**, 20436 (2016).
39. Baily, S. A. et al. Pseudoisotropic upper critical field in cobalt-doped $SrFe_2As_2$ epitaxial films. *Phys. Rev. Lett.* **102**, 117004 (2009).
40. Cho, K. et al. Anisotropic upper critical field and possible Fulde-Ferrel-Larkin-Ovchinnikov state in the stoichiometric pnictide superconductor LiFeAs. *Phys. Rev. B* **83**, 060502(R) (2011).
41. Maiorov, B. et al. Inversion of the upper critical field anisotropy in FeTeS films. *Supercond. Sci. Technol.* **27**, 044005 (2014).
42. Kang, S. et al. High-performance high-T_c superconducting wires. *Science* **311**, 1911–1914 (2006).
43. Eley, S., Miura, M., Maiorov, B. & Civale, L. Universal lower limit on vortex creep in superconductors. *Nat. Mater.* **16**, 409–413 (2017).
44. Xu, A. et al. Angular dependence of J_c for YBCO coated conductors at low temperature and very high magnetic fields. *Supercond. Sci. Technol.* **23**, 014003 (2010).
45. Tallon, J. L., Loram, J. W., Cooper, J. R., Panagopoulos, C. & Bernhard, C. Superfluid density in cuprate high-T_c superconductors: a new paradigm. *Phys. Rev. B* **68**, 180501(R) (2003).
46. Hashimoto, K. A sharp peak of the zero-temperature penetration depth at optimal composition in $BaFe_2(As_{1-x}P_x)_2$. *Science* **336**, 1554–1557 (2012).
47. Joshi, K. R. et al. Quantum phase transition inside the superconducting dome of $Ba(Fe_{1-x}Co_x)_2As_2$ from diamond-based optical magnetometry. *New J. Phys.* **22**, 053037 (2020).
48. Sakurai, R. et al. Quantum critical behavior in heavily doped $LaFeAsO_{1-x}H_x$ pnictide superconductors analyzed using nuclear magnetic resonance. *Phys. Rev. B* **6**, 064509 (2015).
49. Sadovskyy, I. A., Koshelev, A. E., Kwok, W., Welp, U. & Glatz, A. Targeted evolution of pinning landscapes for large superconducting critical currents. *Proc. Natl Acad. Sci. USA* **116**, 10291–10296 (2019).
50. Sun, Y. et al. Enhancement of critical current density and mechanism of vortex pinning in H^+-irradiated FeSe single crystal. *Appl. Phys. Express* **8**, 113102 (2015).

[1]Graduate School of Science and Technology, Seikei University, Tokyo, Japan. [2]National High Magnetic Field Laboratory, Los Alamos National Laboratory, Los Alamos, NM, USA. [3]Fusion Oriented REsearch for disruptive Science and Technology (FOREST), Japan Science and Technology Agency (JST), Tokyo, Japan. [4]Department of Electrical & Computer Engineering, University of Washington, Seattle, WA, USA. [5]Department of Physics, Colorado School of Mines, Golden, CO, USA. [6]College of Industrial Technology, Nihon University, Chiba, Japan. [7]Laboratory for Materials and Structures, Institute of Innovative Research, Tokyo Institute of Technology, Yokohama, Japan. [8]MDX Research Center for Element Strategy, International Research Frontiers Initiative, Tokyo Institute of Technology, Yokohama, Japan. [9]Department of Basic Science, The University of Tokyo, Tokyo, Japan. [10]Kwansei Gakuin University, Sanda, Japan. [11]The Institute of Advanced Sciences, Yokohama National University, Yokohama, Japan. [12]Department of Electrical and Electronic Engineering, University of Yamanashi, Kofu, Japan. [13]Nanostructures Research Laboratory, Japan Fine Ceramics Center, Nagoya, Japan. [14]Institute for Materials Research, Tohoku University, Sendai, Japan. [15]Takasaki Institute for Advanced Quantum Science, National Institutes for Quantum Science and Technology (QST), Takasaki, Japan. [16]Institute for Technical Physics, Karlsruhe Institute of Technology, Eggenstein-Leopoldshafen, Germany. [17]National Institute for Materials Science (NIMS), Tsukuba, Japan. ✉e-mail: masashi-m@st.seikei.ac.jp

Methods

Sample preparation

The undoped SmFeAsO epitaxial films on MgO(001) single crystals were grown by pulsed laser deposition to a thickness of 50 nm. Film thickness was measured using a step profiler and confirmed using cross-sectional transmission electron microscopy. Doped $SmFeAsO_{1-x}H_x$ epitaxial thin films were prepared by topotactic chemical reaction between the undoped SmFeAsO epitaxial film and CaH_2 powder. More details regarding the growth method, describing the pulsed laser deposition process and thermal annealing, can be found in ref. 20. The $NdFeAsO_{1-x}H_x$ and $NdFeAsO_{1-x}F_x$ epitaxial films were grown on MgO(001) single crystals using molecular beam epitaxy[24]. The Y123 nanocomposite films were grown epitaxially from metal organic solutions[3]. Lastly, both the $BaFe_2(As_{1-x}P_x)_2$ and the $FeSe_{1-x}Te_x$ (ref. 15) epitaxial films were deposited using pulsed laser deposition.

Ion irradiation of the $SmFeAsO_{1-x}H_x$ thin films was performed using the 400 kV ion implanter at the Takasaki Ion Accelerators for Advanced Radiation Application facility of the Takasaki Institute for Advanced Quantum Science (QST). Proton beams of energy 150 keV were directed at the film surfaces at normal incidence and a fluence of 5.3×10^{14} ions cm^{-2}.

Transport properties in magnetic fields

The films were patterned using a pulsed fibre laser into bridges of ~30 μm width. The temperature dependence of the resistivity (ρ) was measured by a four-probe method in the temperature range of 4–300 K using a Physical Property Measurement System with a superconducting magnet generating a field **H** up to 9 T and in a 25 T superconducting magnet at Tohoku University. The critical current density was determined using a 1 μV cm^{-1} criterion. The resistivity criterion for determining H_{c2} is 80% of the temperature dependence of the normal state resistivity ($\rho_N(T)$) which is extrapolated from the available $\rho_N(T)$ up to just above T_c^{onset}. We compared our data in Fig. 5c to data reported by Hanzawa et al.[22] and thus chose the same metric for extracting H_{c2}. Similarly, H_{irr} was determined using 1% of $\rho_N(T)$. Hall measurements were conducted in a magnetic field of 9 T, and magnetization studies were performed using a superconducting quantum interference device (SQUID) magnetometer to characterize the temperature and field dependence of S.

Data availability

The data that support the findings of this study are available from the corresponding author on reasonable request. Source data are provided with this paper.

Acknowledgements

H. Hiramatsu and H. Hosono were supported by the Ministry of Education, Culture, Sports, Science, and Technology (MEXT) through the Element Strategy Initiative to Form Core Research Center (grant no. JPMXP0112101001). This work at Seikei University was supported by the Japan Science and Technology Agency (JST) Fusion Oriented REsearch for disruptive Science and Technology (FOREST; grant no. JPMJFR202G, Japan). A part of this work at Seikei University was supported by Japan Society for the Promotion of Science (JSPS) KAKENHI (23H01453). Contributions from Nihon University were supported by JSPS KAKENHI (20H02681). Work by B.M. was performed at the NHMFL, which is supported by National Science Foundation cooperative agreement no. DMR-2128556, the State of Florida and the US Department of Energy (LANL-LDRD). S.E. gratefully acknowledges support from the National Science Foundation (DMR-2330562; formerly DMR-1905909) as well as partial support through the University of Washington, Materials Research Science and Engineering Center (DMR-2308979). We thank S. Iimura for providing a standard polycrystalline bulk sample, $SmFeAsO_{0.4}H_{0.6}$, to perform quantitative chemical composition analysis by SIMS. We also thank T. Harada and H. Saito for conducting the transport measurement; C. Hewson and A. Matthews for conducting magnetization measurements at the Colorado School of Mines; and S. Yamamoto and H. Koshikawa for supporting proton irradiation at QST.

Author contributions

M.M., K.I., H. Hiramatsu and H. Hosono designed the experiment. K.H. analysed the upper critical field data. J.M. and H. Hiramatsu grew the Sm1111 films; K.I. deposited the Nd1111 films; T. Kobayashi and A.M. grew the 11-type films; and M.M. deposited the Y123 and 122-type films. S.E. conducted some magnetization measurements and analysis. M.M., Y.O. and T.S. carried out the transport measurement. T. Ozaki, H.O. and T.Y. carried out the proton irradiation studies. H.K. contributed to the discussion of the penetration depth analysis. N.S. analysed the resonance frequency data. R.Y. and T. Kato performed microstructural studies. T. Okada and S.A. contributed to the discussion of the transport measurements at high fields. B.M. performed data analysis, and B.M., S.E. and J.H. provided advice and consultation on flux pinning. All authors discussed the results and implications and commented on the manuscript. M.M. and S.E. wrote the manuscript with contributions from all authors.

Competing interests

The authors declare no competing interests.

Additional information

Supplementary information The online version contains supplementary material available at https://doi.org/10.1038/s41563-024-01952-7.

Correspondence and requests for materials should be addressed to Masashi Miura.

Peer review information *Nature Materials* thanks Xavier Obradors, Marina Putti and the other, anonymous, reviewer(s) for their contribution to the peer review of this work.